

PAPER

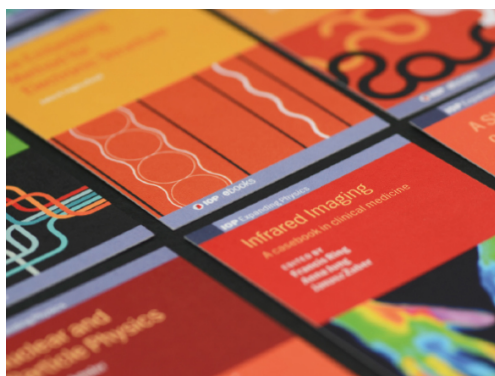
Impurity transport studies at the HSX stellarator using active and passive CVI spectroscopy

To cite this article: C Swee *et al* 2022 *Plasma Phys. Control. Fusion* **64** 015008

View the [article online](#) for updates and enhancements.

You may also like

- [Measurement of a helical Pfirsch–Schlüter current with reduced magnitude in HSX](#)
J.C. Schmitt, J.N. Talmadge and D.T. Anderson
- [The role of neutral friction in governing parallel flows in the HSX stellarator](#)
T.J. Dobbins, S.T.A. Kumar, J.N. Talmadge et al.
- [TEM turbulence optimisation in stellarators](#)
J H E Proll, H E Mynick, P Xanthopoulos et al.



IOP | ebooks™

Bringing together innovative digital publishing with leading authors from the global scientific community.

Start exploring the collection—download the first chapter of every title for free.

Impurity transport studies at the HSX stellarator using active and passive CVI spectroscopy

C Swee^{1,*} , B Geiger¹ , R Dux², S T A Kumar¹, J F Castillo¹, A Bader¹  and M Gerard¹

¹ Department of Engineering Physics, University of Wisconsin, Madison, WI, 53706, United States of America

² Max-Planck-Institute for Plasma Physics, Boltzmannstr. 2, 85748 Garching, Germany

E-mail: ckswhee@wisc.edu

Received 10 August 2021, revised 27 October 2021

Accepted for publication 12 November 2021

Published 29 November 2021



Abstract

The transport of carbon impurities has been studied in the helically symmetric stellarator experiment (HSX) using active and passive charge exchange recombination spectroscopy (CHERS). For the analysis of the CHERS signals, the STRAHL impurity transport code has been re-written in the python programming language and optimized for the application in stellarators. In addition, neutral hydrogen densities both along the NBI line of sight as well as for the background plasma have been calculated using the FIDASIM code. By using the basinhopping algorithm to minimize the difference between experimental and predicted active and passive signals, significant levels of impurity diffusion are observed. Comparisons with neoclassical calculations from DKES/PENTA show that the inferred levels exceed the neoclassical transport by about a factor of four in the core and more than 100 times towards the plasma edge, thus indicating a high level of anomalous transport. This observation is in agreement with experimental heat diffusivities determined from a power balance analysis which exhibits strong anomalous transport as well.

Keywords: impurity, transport, HSX, stellarator, STRAHL, FIDASIM

(Some figures may appear in colour only in the online journal)

1. Introduction

Control of heavy impurities in fusion plasmas is imperative to reliable operation of both experimental devices and future reactors. Light impurities such as helium ash from the fusion process would dilute the fuel in a future fusion reactor and can thereby significantly degrade its efficiency [1]. In addition, heavy impurities, sputtered from the walls can lead to excessive cooling through line radiation from inner shell electrons that remain tightly bound even at fusion relevant temperatures. Thus, the accumulation of impurities inside the plasma must be avoided. However, this is challenging as the physics mechanisms responsible for impurity transport are not yet fully understood. Impurities are subject to both, neoclassical and

anomalous transport which have convective and diffusive contributions that strongly depend on the plasma parameters, as well as on the 3D magnetic field topology. Particularly, in the case of stellarators, the effect of magnetic topology is of great interest due to the presence of an ambipolar electric field that can result in strong inwards directed heavy impurity fluxes for reactor relevant conditions. This is in part why e.g. the helically symmetric experiment (HSX) has been optimized for low neoclassical heat and particle fluxes which might help avoid impurity accumulation. While neoclassical heat transport has been studied in detail at HSX [2], and it has been shown that turbulence driven by trapped electron modes (TEMs) dominates the confinement [3], the impurity transport has not been investigated in detail so far.

For the study of impurity transport, line radiation from either intrinsic impurities sputtered from the vessel walls such

* Author to whom any correspondence should be addressed.

as carbon, or purposely injected impurities such as aluminum [4, 5] can be analyzed. Charge exchange recombination spectroscopy (CHERS) is typically applied to obtain radially resolved information on light impurities. The technique is based on neutral beam injection which provides core-localized donor hydrogen neutrals that undergo charge exchange reactions with fully stripped impurity ions, resulting in characteristic hydrogen-like line radiation. Spectroscopic diagnostics with lines of sight that cross the NBI path at various positions can then be used to gain spatial information. In addition, passive, line-integrated radiation can be observed which is caused by electron impact excitation of impurity ions with electrons, as well as by charge exchange reactions with background hydrogen neutrals. Here, spatial information is limited but is contained in the ionization balance of impurities. Radiation from highly ionized impurities is expected from the hot plasma core while radiation from low charge states typically dominates at the cold plasma edge region.

For the interpretation of active and passive spectroscopy measurements, forward modelling codes such as STRAHL can be used [4, 6, 7]. STRAHL requires background plasma profiles, a geometric grid on which the calculation is done, and tabulated rate coefficients for ionization, recombination, and charge exchange. The code then solves the 1D coupled impurity transport equation (equation (1)) and provides impurity densities as a function of time and position:

$$\frac{\partial \vec{n}}{\partial t} = \frac{1}{r} \frac{\partial}{\partial r} r \left[\hat{D}(r) \frac{\partial \vec{n}}{\partial r} - \hat{v}(r) \vec{n} \right] - \hat{S} \vec{n} - \hat{R} \vec{n} + \vec{d}. \quad (1)$$

Here, \vec{n} is the number density of each ionization stage, \hat{D} and \hat{v} are diagonal matrices containing the transport coefficients. \hat{S} and \hat{R} are matrices with the ionization and recombination rates respectively for each ionization stage and as functions of position. Finally, \vec{d} is the source term for ionization of neutral impurities and is zero for all elements except the index corresponding to the unionized stage. The matrix equation is then solved numerically via an iterative algorithm described in detail in the STRAHL user manual [8].

The calculated evolution of the 1D impurity density can either be compared directly with experimental impurity densities, as obtained from CHERS, or be used to predict synthetic line-integrated signals. For the latter, tabulated photo-emission coefficients [9] are used to provide simulated emission data as functions of time and position.

In this work, we present a detailed impurity transport study of carbon impurities at the HSX optimized stellarator experiment. Such impurities are present in the walls due to carbon conditioning and are subsequently intrinsic to the generated plasmas. To aid in simulation efforts, recent developments have been made to optimize the use of STRAHL in stellarator contexts. A fully python based implementation of STRAHL has been developed that is closely coupled to the pyFIDASIM code which provides information on background and beam neutral hydrogen densities. By analyzing active and passive radiation measured by the HSX CHERS system, the

reconstruction of impurity diffusion profiles at HSX became possible for the first time.

Section 2 discusses the aforementioned improvements to the STRAHL code and presents results of a bench-marking exercise. In sections 3–5 the study of the carbon impurity transport in HSX is presented. Finally, in section 6 a discussion of simulation results is presented and an outlook for future work is provided.

2. Description of the pySTRAHL Code

2.1. Python STRAHL implementation and benchmarking

The original STRAHL code is written in Fortran77, a programming language mainly used in the 1980s which is highly optimized for speed and is still utilized in many scenarios where computation run time is important. Since then, however, more user friendly programming languages have been developed which offer simplified software development and a broad library of packages for data analysis. For the optimization of STRAHL with respect to impurity transport studies in stellarators, the code has therefore been converted into the python programming language.

The numba library is utilized to compile the python code into C at runtime. Numba uses compilers intrinsically available both in Windows and Linux and speeds the code up by up to a factor of 50, eventually providing speeds comparable to those achievable via the Fortran implementation.

The new python version of STRAHL, here referred to as ‘pySTRAHL’, has been benchmarked by comparing calculated impurity densities to those calculated using the original Fortran code.

For the benchmarking, we chose the case that will be discussed in sections 3 and 4. Carbon is fueled continuously into a representative plasma experiment at HSX, characterized by plasma profiles shown in figure 6. Moreover, the neo-classical convection and anomalous diffusion profiles plotted in figure 8, as well as a parallel loss times based on known connection lengths and the EMC3-EIRENE calculated parallel flow velocity are considered.

Figure 1 compares the impurity densities predicted by the Fortran and python codes for a time point at which the impurity profiles have reached equilibrium state. The profiles are plotted as a function of the normalized effective radius and are given for all six charge states of carbon. The agreement between the two codes is excellent with differences of only about 1 percent or lower for all charge states. Note that this benchmark considers all subroutines of STRAHL and not only the core routine, i.e. the code which solves the impurity transport equation. These subroutines include the generation of the simulation grid, fetching the ionization, charge exchange, and recombination rates, and calculating ionization profiles of incoming neutral impurities. When only comparing results for the core routine, differences between the two codes are below 0.01 percent, indicating that the larger differences of ~1%

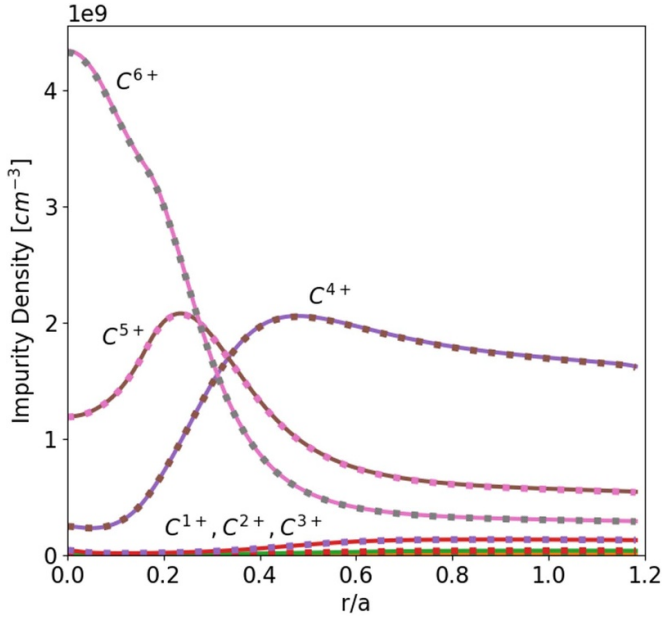


Figure 1. Comparison of impurity charge state distributions calculated using pySTRAHL (solid lines) and the fortran version of STRAHL (dotted lines). Shown is the case resulting from the fit described in section 4.

originate from slight differences in the interpolation schemes used by the FORTRAN and python codes.

2.2. pySTRAHL for stellarator geometries

When using STRAHL for stellarator geometries, several aspects need to be considered. First, STRAHL is a 1D transport code which assumes cylindrical geometry. In contrast, and for accurate 3D mapping, pySTRAHL has been supplied with 3D VMEC equilibria, which allow the calculation of effective radii, a_{eff} , based on the volume V of a given flux-surface and the major radius R :

$$a_{\text{eff}} = \sqrt{\frac{V}{2\pi^2 R}}. \quad (2)$$

Subsequently, the effective radii are used to map kinetic profiles onto the STRAHL simulation grid. Note here, that the kinetic plasma profiles are assumed constant on the flux surfaces in the confined region which justifies a 1D approach. To additionally cover the SOL region in STRAHL, the VMEC equilibria (only defined for closed flux surfaces) are extended by quadratically extrapolating the volume enclosed by the flux surfaces and maintaining the flux surface shape. The corresponding extrapolated surfaces can then be used to map 3D SOL profiles onto the 1D radial grid of STRAHL by taking a spatial average over the 3D surfaces. For this work, 3D SOL profiles from a representative EMC3-EIRENE [10] simulation are used. This code couples the plasma transport code EMC3, to the neutral gas kinetic simulation EIRENE, and allows the prediction of 3D kinetic profiles and neutral hydrogen densities to be considered in STRAHL.

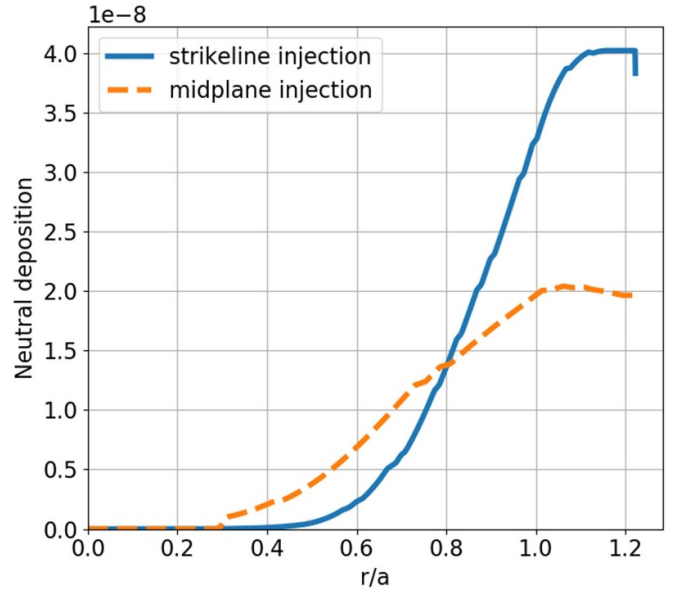


Figure 2. Neutral deposition profiles of carbon impurities for two different 3D injection paths into the HSX stellarator.

Secondly, and as mentioned before, STRAHL calculates 1D radial ionization profiles of incoming impurities. As impurities impinge from the edge, they necessarily become ionized at a rate set by the local ionization frequency. The attenuation of the incident population of neutral impurities is exponential within each radial grid point, with a decay constant set by the local ionization rate and the speed of the impurities. These ‘deposition’ profiles depend on the local temperature and density along the sourcing direction and, in case of a localized impurity source, require the consideration of the 3D structure. As an example, figure 2 shows the ionization profile of carbon impurities that enter the plasma close to the strike-line, vs impurities entering from the midplane position in the so-called bean shaped cross-section of HSX (see figure 3). Clearly, the impurity deposition profile is more outwards shifted in case of the strike-line injection, explained by a stronger flux surface spacing such that impurities travel longer distances before reaching the core. Note that an impurity source close to the strike-line is most likely for intrinsic impurities in HSX. Therefore, this impurity ionization profile has been implemented for the study presented in section 4. Moreover, it should be noted that the 3D ionization profile is of great importance in the case of laser blow off injection. An example depicting the difference in neutral impurity deposition profiles for cylindrical and realistic geometries is discussed in the [appendix](#).

Next, information on the neutral hydrogen density is required in two contexts. First, 1D neutral densities are used in STRAHL to determine charge exchange recombination rates which contribute to the charge state balance (a summary of reaction rates is given in the [appendix](#)). Secondly, 3D neutral density profiles are used when modelling the charge exchange radiation present along synthetic diagnostic lines of sight. For this reason, pySTRAHL has been coupled to the FIDASIM code, which is a 3D Monte Carlo (MC) particle

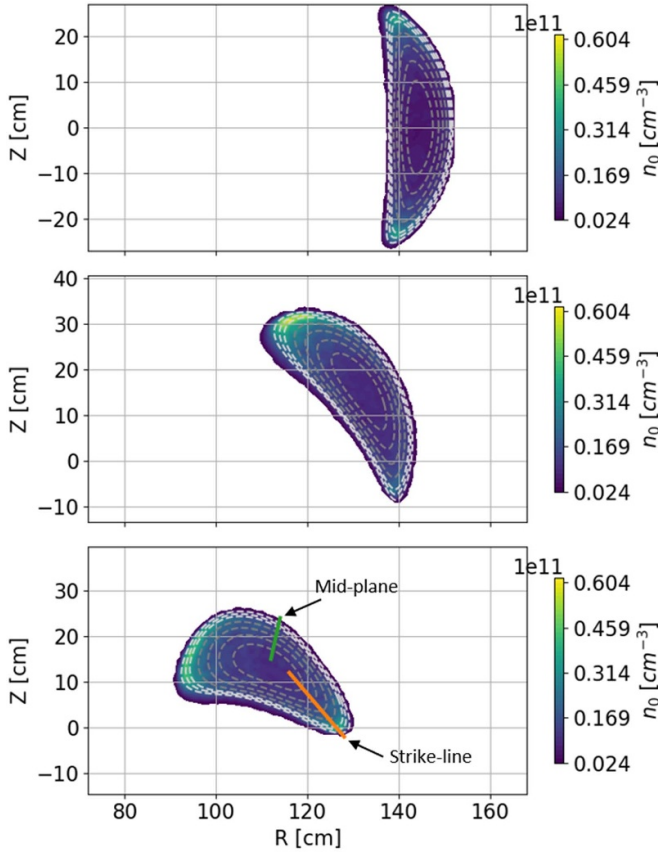


Figure 3. 3D neutral hydrogen density profile calculated using pyfidasim. Shown at toroidal positions of 0 (Top), 15 (Middle), and 30 (Bottom) degrees. Confined flux surfaces are shown in grey dashed lines while 'extrapolated' flux surfaces are shown in white dashed lines. The bottom plot additionally shows the geometry of the neutral carbon deposition path coming from the strike-line (orange) and the mid-plane (green).

simulation code, originally developed to predict the neutral density along neutral beam injection paths [11–13]. However, it has recently been upgraded to predict 3D neutral hydrogen density profiles by launching neutrals from the plasma boundary and simulating their trajectory, including the change of velocity vectors in presence of charge exchange reactions. When launching neutrals from the boundary, the 3D neutral hydrogen density distribution from EMC3-EIRENE is used to define values on the LCFS. Moreover, the absolute neutral densities are set by a particle confinement time, which needs to be provided as input and can be regarded as a free parameter.

An example FIDASIM-predicted neutral hydrogen density distribution (500 000 simulated particles) is shown in figure 3. One can note here the effect of the 3D geometry of HSX which causes an asymmetry in the neutrals in both the poloidal and toroidal direction. This distribution can then be flux surface averaged to generate a 1D profile as plotted in figure 4. Note here that FIDASIM provides neutral hydrogen densities for excited states up to $n = 6$. This is important since the $n = 2$ excited level of hydrogen neutrals contributes significantly e.g. to passive charge exchange radiation of carbon ions.

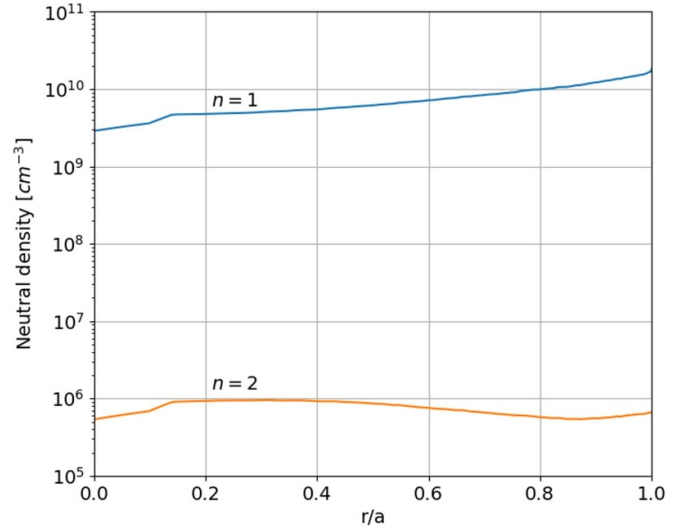


Figure 4. Flux surface averaged neutral densities for $n = 1$ and $n = 2$ states of neutral hydrogen calculated using FIDASIM. Note the absolute magnitudes of these profiles are not resolved, only the relative shapes.

Moreover, it should be noted that the approach using a representative EMC3-Eirene edge-neutral hydrogen distribution as input to FIDASIM is justified as the shape of the edge distribution of neutrals is dominated by the flux-surface shape and vessel geometry and does not strongly depend on plasma conditions.

3. Experimental setup at HSX

At HSX, pySTRAHL has been applied to study the transport of intrinsic carbon impurities based on active and passive CVI signals. HSX is characterized by a major radius of 1.2 m, a minor radius of 12 cm, and an on-axis magnetic field of ~ 1 T. The quasi-helical symmetric (QHS) magnetic field is defined by 48 main coils with 4-fold periodicity.

For the experiment described here 28 GHz Electron Cyclotron Resonance Heating (ECRH) is applied with ~ 50 kW of injected power of which ~ 15 kW is absorbed. Representative time traces of the 50 ms long experiment are given in figure 5, showing the line averaged density, radiated power, and measured stored energy [14].

Radial profiles of the electron temperature and density, as measured by a Thomson scattering diagnostic, are shown in figure 6. The data represents an average over 12 consecutive experiments taken on 2 February 2017 (shots 19–31) as the uncertainties of a single experiment are too large. The experimental electron temperature profile data has been fit by the following function

$$T_e = ae^{-b(r-c)^2} \quad (3)$$

and the electron density has been fit by:

$$n_e = a(1 - r^2)^b + c. \quad (4)$$

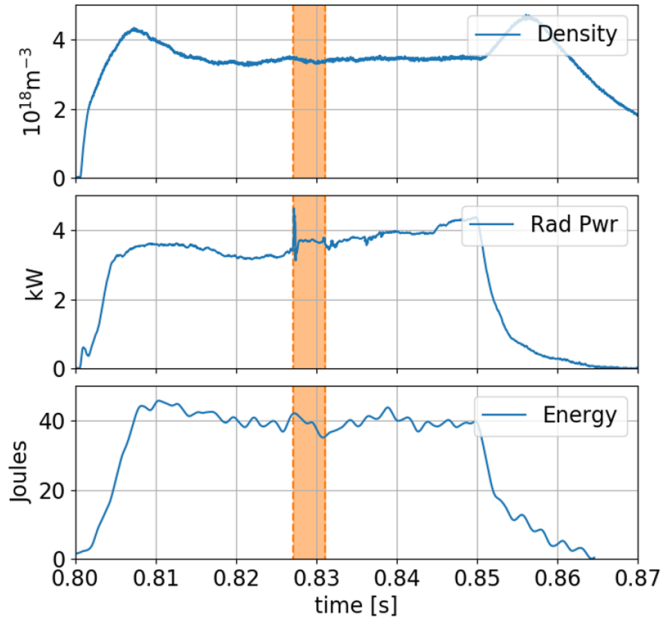


Figure 5. Time traces of the line averaged density (top), radiated power (middle), and stored energy (bottom) for shot taken 2 February 2017 (shot number 19). The time span where the diagnostic neutral beam is on is shaded in orange.

This provides smooth electron temperature and density profiles which can be extended in the SOL region by the aforementioned 1D averaged EMC3-Eirene predicted profile shape.

The ion temperature profiles in HSX are typically flat with values of ~ 50 eV in the confined region [15]. This is explained by a weak coupling between the heated (ECRH) electrons and ions and due to charge exchange losses.

To determine the ambipolar electric field and neoclassical diffusion and convection profiles of impurity ions, the kinetic moment solver PENTA [16] is used. PENTA considers mono-energetic transport coefficients from DKES database files collected for the QHS magnetic geometry. The resulting ambipolar electric field is then given in figure 6. As can be seen, the electric field is positive in the core plasma (electron root) and is expected to be negative (ion-root) in the region with $r/a > 0.2$.

The corresponding calculated neoclassical convection and diffusion profiles are shown in figure 8. Mostly due to the neoclassical optimization of the HSX stellarator, both the diffusive and convective contributions are relatively small. The diffusion is only on the order of $10^{-3} \text{ m}^2 \text{ s}^{-1}$ and the absolute value of the convective drift does not exceed 1 m s^{-1} . Note here that the shape of the convection profile is dominated by the ambipolar electric field and is outwards directed in the core region and inwards directed towards the edge.

For charge exchange recombination measurements, a diagnostic neutral beam with 3 ms pulse-length is available. This beam injects hydrogen neutrals with an injection energy of 28 keV, a current of 4 A, and with 94% of the neutrals at the full energy. Two Czerny-Turner spectrometers are then able to analyze the radiation collected by 20 lines of sight intersecting the neutral beam at various spatial positions [17]. For the

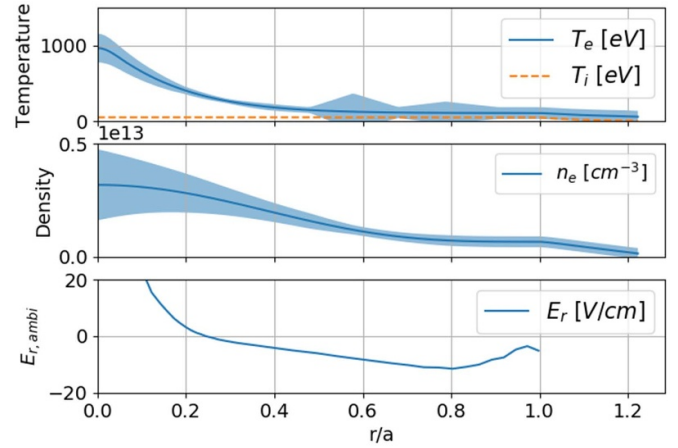


Figure 6. Kinetic profiles utilized in STRAHL simulation of Carbon impurity transport along with PENTA calculated ambipolar radial electric field. Error bands are a quadrature sum of Thomson scattering measurement error and error estimated from the least squares fit used for fitting to analytic profiles.

experiment described in this work, passive CHERS signals are collected at the time stamp of ~ 0.82 s, while the active signal is collected at ~ 0.83 s (see figure 5).

4. Simulation of active and passive CVI emission profiles at HSX

The active CVI emission profile (shown in figure 7) can be inverted into a C^{6+} density profile using the FIDASIM code. FIDASIM simulates the neutral beam attenuation and density and therefore allows using tabulated CVI emission rates to calculate the expected CVI emissivity per impurity ion. Figure 8 shows the resulting carbon impurity density profile. In addition, the line-integrated passive CVI emission, present due to both electron impact excitation of C^{5+} and charge exchange of C^{6+} is shown in figure 8. This passive emission profile can be compared to pySTRAHL simulations when considering 3D neutral hydrogen densities and the 3D geometry of the employed spectroscopy system.

For the pySTRAHL modelling the above mentioned kinetic profiles, as well as the 1D and 3D neutral hydrogen density profiles from FIDASIM, are used. To model the charge state distribution and impurity profile under equilibrium conditions (expected since the radiated power is roughly constant during the analyzed experiment), pySTRAHL is set to simulate a constant impurity source rate and to simulate for 5 s (~ 100 times longer than a typical HSX discharge). Note that in cases considering strong diffusive transport, steady state is reached much faster than 5 s.

Considering the plasma conditions at HSX, we can check whether the 1D approach for modeling impurity transport is valid. As discussed in [18], STRAHL's 1D approximation is valid when the transport time along a flux surface is much shorter than the ionization time for a given impurity. The ratio of the ionization time to the transport time is then (equation (5)):

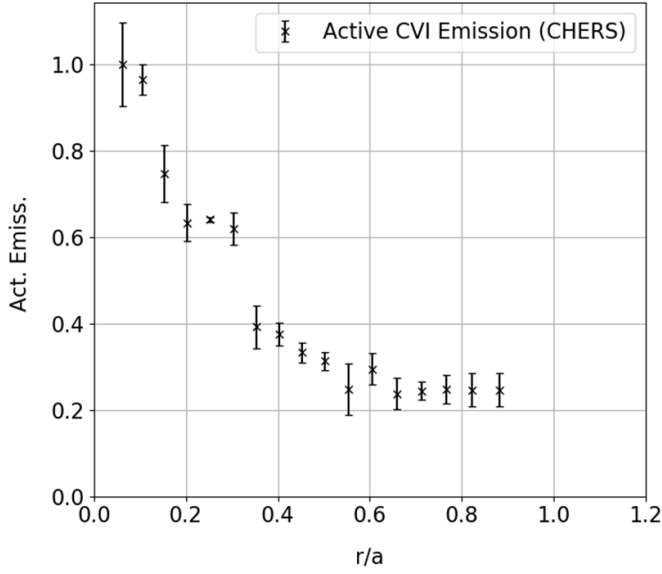


Figure 7. Active C^{6+} signal (normalized) as measured by the CHERS diagnostic.

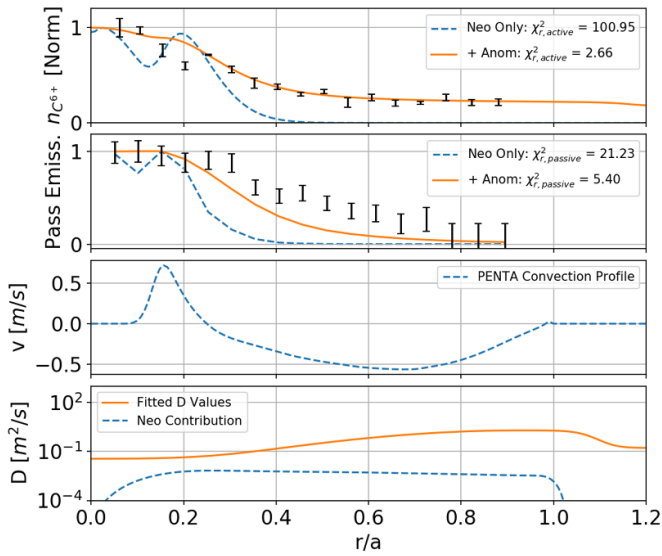


Figure 8. Active and passive measurements for comparison to forward model (shown in black with error bands). Additionally shown is basinhopping fit results for the case of diffusion and convection fixed to neoclassical prediction (shown in blue), as well as fit results where an additional anomalous diffusion component is allowed to vary (shown in orange).

$$\nu_{ion,z}^* = \nu_{ion,z} \tau_t = \frac{\nu_{ion,z} R}{\tau v_{th}} \quad (5)$$

Here, ν_z^{ion} is the ionization frequency of an impurity at charge state z . v_{th} is the thermal velocity of the impurity ion and τ is the rotational transform. If this ratio is much less than one, the impurities ionize much slower than the time it takes for their densities to equilibrate along a given flux surface. This ratio is calculated for the impurity densities found as a result of the global minimization scheme described in sections 4 and 5 and

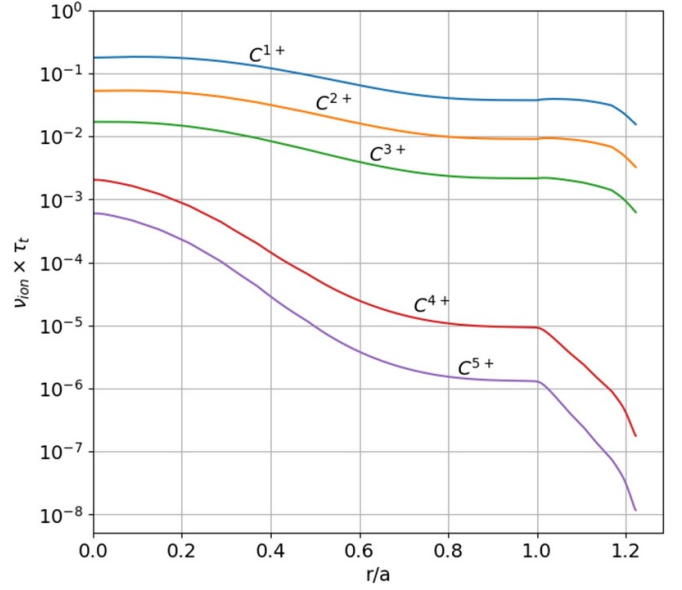


Figure 9. Ratio of impurity transit time along a flux surface to the ionization time for various Carbon charge states.

is described in figure 9. The ratio is well below 1 for all charge states, thus justifying the 1D approach.

5. Fit results

5.1. Initial fit results

The ‘basinhopping’ global minimization scheme is utilized to minimize the difference between simulated and measured active and passive CVI signals. Several free parameters are considered as detailed below.

First, the impurity influx is allowed to vary since the absolute magnitude of incident carbon is unknown. In addition, this allows the code to intrinsically account for the additional influx due to recycling from the wall/limiter.

Secondly, a scaling factor for the neutral hydrogen density is considered as a free parameter since the calculation of the neutral profile, described in section 2, does not resolve the absolute magnitude. This will of course affect both the charge state balance (due to the additional recombination mechanism introduced by charge exchange) as well as the shape and magnitude of the passive charge exchange signal. With these two parameters, it is possible to assess whether the neoclassical diffusion and convection profiles can explain the profile shapes of the C^{6+} density and passive CVI emission, as obtained in the experiments.

As a pre-processing step, it was necessary to smooth the input diffusion and convection profiles from PENTA using a moving average filter since overly strong (and nonphysical) gradients can lead to a numerical instability in the pySTRAHL code. The resulting profiles following neoclassical transport are shown in blue in figure 8. As can be seen, the agreement is poor, also reflected by a large residual χ^2 value. The neoclassical transport would cause a strong peaking of the CVI

density outside the core region, as well as a strongly peaked passive CVI emission which is not observed.

In order to assess the additional level of transport necessary to reproduce synthetic diagnostic signals in agreement with measurement, an anomalous diffusion profile, described by five free parameters has been introduced. This diffusion profile is determined by a hyperbolic tangent curve at the plasma edge and an exponential decay toward the center. The free parameters which describe this diffusion profile are then the value and location of the maximum, the decay length toward the center, and the values in the core and edge. This specific form for the diffusion was chosen due to its flexibility in shape as well as being described by a relatively small number of free parameters.

Note here, that no anomalous convection is considered as it has been shown that from gyrokinetics calculations that this component is small compared to the Fickian diffusion contribution [19]. Also, the introduction of additional free parameters for the convection profile would significantly slow down the fitting algorithm.

In summary, seven free parameters have been considered in the fitting results discussed below: five determine the diffusion profile shape, one determines the carbon impurity influx, and one determines absolute magnitude of the 1D and 3D neutral hydrogen profiles.

The fitted density profile, passive emission profile and corresponding diffusion profile are shown in figure 8. The fitted influx rate is found to be $\sim 5.2 \times 10^{20} \text{ cm}^{-1} \text{ s}^{-1}$ (note these units are such that when multiplied by the impurity neutral deposition profile, a C^{1+} density as a function of time and position is defined) and the neutral hydrogen scaling factor is found to sit against the lower bound set for the fitting algorithm at 10^{-3} resulting in a ground state neutral density of $\sim 2.5 \times 10^7 \text{ cm}^{-3}$ towards the plasma edge (determined by scaling the profiles shown in figure 4).

Good agreement between data and simulation is obtained by the fitted diffusion profile that is about two orders of magnitude larger than what is expected based on the neoclassical theory. Note that even in the core region where the diffusive transport is at its lowest, the inferred values are at least a factor of four larger than the expected neoclassical contribution.

In addition to the global minimum, one can assess the level of confidence in the trend of the diffusion profile by looking at the various distinct local minima recorded by the basin hopping global optimizer. Figure 10 shows the diffusion profiles for the 15 lowest determined local minima given in grey. Note in some cases, the local minima differ only by the neutral scaling factor and influx rate and are plotted over one another (therefore shown in bolder grey). Also note that the single outlier diffusion profile has a reduced chi squared nearly double that of the global minimum. From this, it becomes clear that there is no solution which would provide good agreement between the experimental data and the simulation when considering only neoclassical transport.

This is further supported as the expected equilibration time of the total impurity content would be close to 170 s under neoclassical conditions (compared to about 160 ms in the case of an additional anomalous contribution), implying that we

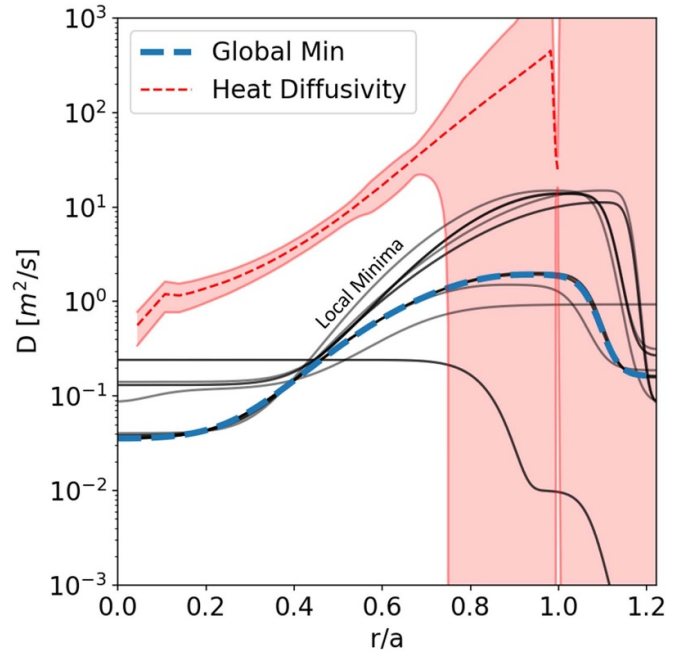


Figure 10. Resulting diffusion profiles for global minimum and 15 lowest local minima of $\chi_{r,\text{passive}}^2 + \chi_{r,\text{active}}^2$. Also plotted is the heat diffusivity as calculated by a power balance analysis on the experimental kinetic profiles.

would have continuous accumulation of impurities over the course of the discharge. Since a strong increase in the radiated power over time is not observed for this experiment, the case of extremely long equilibration time can be ruled out.

It should be noted that the passive CHERS signal was found to have a very strong dependence on the electron temperature in the outer region of the plasma ($r/a > 0.3$). This is due to the charge state balance changing rapidly in the $T_e \sim 100 \text{ eV}$ range even when considering variation inside of the measurement error. A detailed analysis of this dependence is provided in the appendix which shows that the aforementioned statement still holds.

5.2. Comparison with calculated heat diffusivities

The observation of strong anomalous impurity transport in the outer plasma regions is in good agreement with the observation of strong anomalous heat diffusivities.

The electron heat diffusivity can be calculated considering the electron heat flux due to the ECRH heating power density, P_{heating} , the electron to ion heat exchange power density, P_{e-i} , and the radiated power density P_{rad} . Using these quantities, the electron heat flux can be calculated by integrating over the plasma volume:

$$q_e = \int_{r/a} \frac{(P_{\text{heating}}(r/a) - P_{e-i}(r/a) - P_{\text{rad}}(r/a))}{S(r/a)} dV. \quad (6)$$

Here S is the surface area of the flux surface determined by r/a . The volume differential and surface area terms can be determined from a VMEC equilibrium. In our case, P_{heating} is due to ECRH for which the deposition profile has been calculated

via the ray tracing code, TRAVIS [20, 21]. The heat diffusivity then is calculated from the gradient of the measured temperature profile via [22]:

$$\chi_e = \frac{q_e}{-n_e \nabla T_e}. \quad (7)$$

The resulting diffusivities from this calculation are shown in figure 10.

Note here that the very large values towards the edge are a result of the analytic fitting function used to define the T_e profile. Nevertheless, the heat diffusivity exhibits a very similar trend compared to the impurity diffusion profile. It strongly increases towards the plasma edge with values that are much larger than what is expected from neoclassical theory. This suggests that the impurity transport might be dominated by a similar anomalous transport mechanism as the electron heat transport is. In fact, previous publications [3] have shown that electrostatic turbulent fluctuations driven by TEMs are most likely responsible for the strong anomalous heat transport in HSX. Since this type of turbulence is known to drive anomalous particle transport [23, 24], it is a likely candidate to explain the strong anomalous impurity transport observed here.

6. Summary and outlook

Radially resolved impurity diffusion profiles have been reconstructed for the first time at the HSX stellarator, which has been made possible thanks to the development of the pySTRAHL code package. PySTRAHL is a python version of the STRAHL code which has been further optimized for the application in stellarator geometries. The python code has been successfully benchmarked and embedded in the minimization routine. Fitted anomalous diffusion profiles support the hypothesis that the particle transport in HSX is dominated by anomalous contributions since neoclassical predictions can not explain the experimental data obtained from a charge exchange diagnostic. The shape of the obtained impurity diffusion profile resembles that of anomalous heat diffusivity profiles which suggest that impurity transport may be driven by electrostatic turbulent fluctuations. With the modeling framework in place, future analysis of transport at HSX can be carried out. Notable tasks include analysis of the transport in the so-called ‘mirror configuration’ with broken quasi-symmetry and higher levels of neoclassical transport.

Data availability statement

The data that support the findings of this study are available upon reasonable request from the authors.

Acknowledgments

Data and routines depicted in this publication are available upon reasonable request to the author. This work was supported by the U.S. Department of Energy under Contract Nos. DE-SC0020990 and DE-FG02-93ER54222.

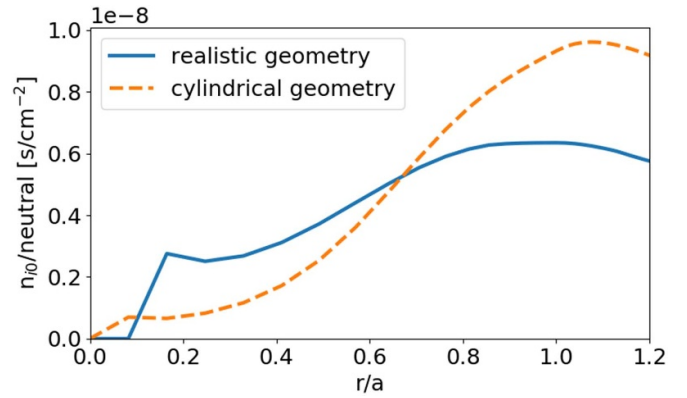


Figure 11. Neutral deposition profile for laser blow off of aluminum into the HSX discharge. Assuming normal incidence on cylindrical flux surfaces (orange) and taking into account 3D flux surface shapes with realistic LBO orientation (blue).

Appendix A. Neutral carbon deposition profile

In the original version of STRAHL, an assumption of cylindrical flux surfaces is utilized for the calculation of the impurity deposition profile, for instance from laser-blow-off. However, this assumption is often not justified in stellarators as flux surfaces are often characterized by higher degrees of elongation. A comparison of a neutral carbon deposition profile calculated via the original STRAHL method as well as one from pySTRAHL is shown in figure 11. Here, we consider the 3D flux-surface and LBO injection geometry for HSX.

Appendix B. Ionization, recombination, and charge exchange rates

Rates for the ionization, recombination, and charge exchange processes are necessary for the solution to the impurity transport equation (see equation (1)). These rates are available as a function of temperature, density, and charge state and have been tabulated in the ADAS database [9]. One then only needs to interpolate the rates onto the experimental profiles used in the simulation. The corresponding values for the studies presented in this work are depicted in figure 12.

Appendix C. Temperature sensitivity study

The passive CHERS signal is composed of charge exchange and electron impact excitation radiation. While the charge exchange radiation depends on the C^{6+} density, the electron impact contribution scales with the C^{5+} density. The abundance of the two charge states scales strongly with the electron temperature profile. Figure 13 shows results based on a corona model prediction, considering the balance between the ionization and recombination rates, while neglecting radial transport.

As can be seen, the region surrounding $T_e = 100$ eV transitions very quickly from being dominated by C^{6+} to C^{5+} to

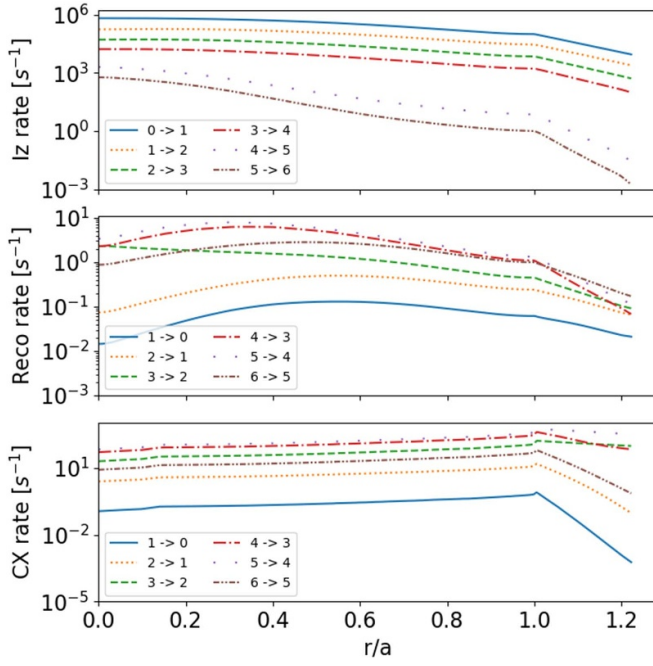


Figure 12. Ionization, recombination, and charge exchange rates for the kinetic profiles given in figure 6.

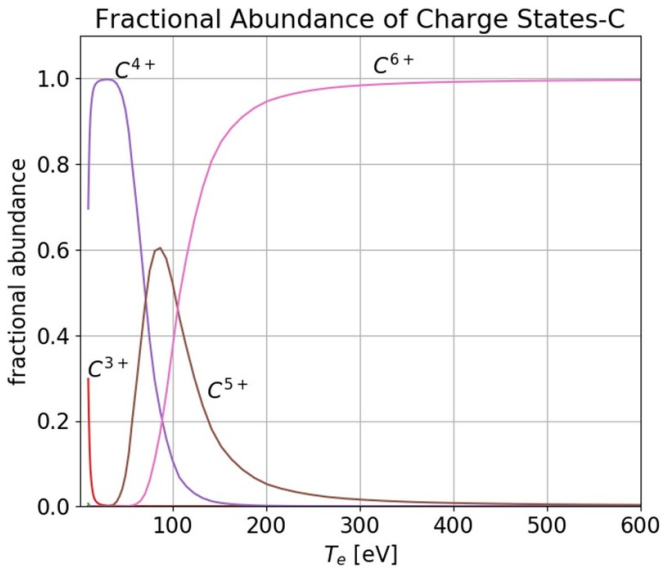


Figure 13. Corona model prediction of charge state distribution of Carbon as a function of temperature (assuming $n_e = 2 \times 10^{12} \text{ cm}^{-3}$).

C^{4+} . This temperature region is in fact spanned by the measurement error around the experimental T_e profiles outside of r/a 0.6. For this reason, a scan of the fit result sensitivity on the temperature profile was carried out. For this analysis, an additional uniform offset is given to the fitted temperature profile before the minimization scheme is carried out. The results of this exercise are shown in figures 14–16.

As expected from the coronal equilibrium prediction, the calculated passive emission signal, and the corresponding quality of fit are highly dependent on the temperature profile.

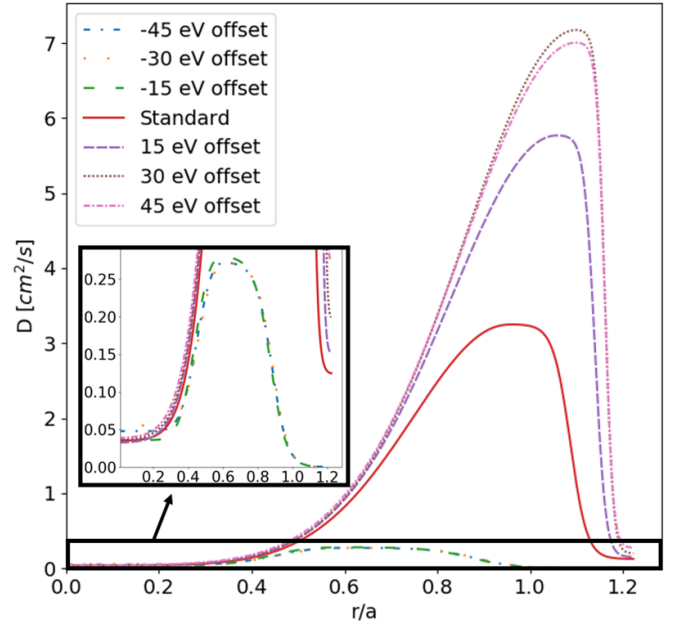


Figure 14. Best fit diffusion profiles for various additional temperature offsets.

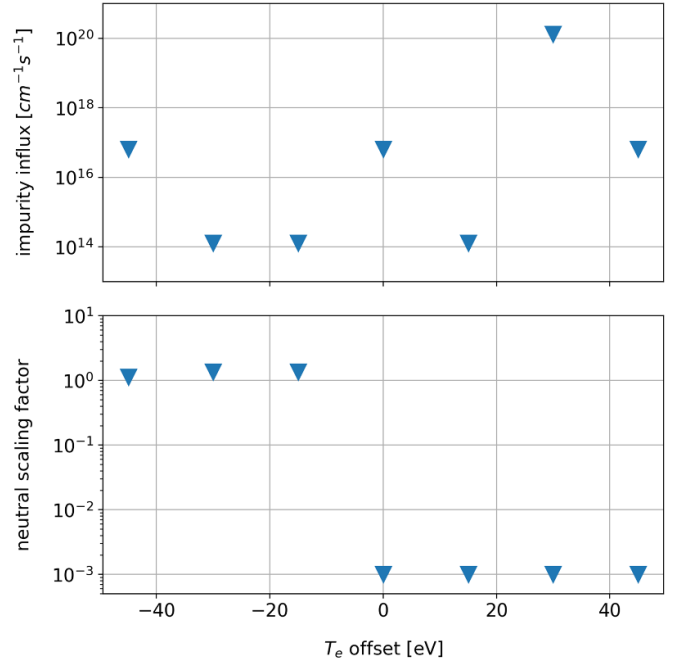


Figure 15. Fitted values for impurity influx and the neutral hydrogen scaling factor.

This can be seen in figure 16 where the quality of fit for the passive chi squared signal improves for larger offsets. While the quality of best fit varies in each of these temperature cases, the general trend of the fitted diffusion profiles remain similar. That is, the core consists of a region of smaller diffusion while diffusion increases towards the edge. In addition, each of these cases is described by a level of diffusion in the core at least a factor of two larger than the neoclassical contribution.

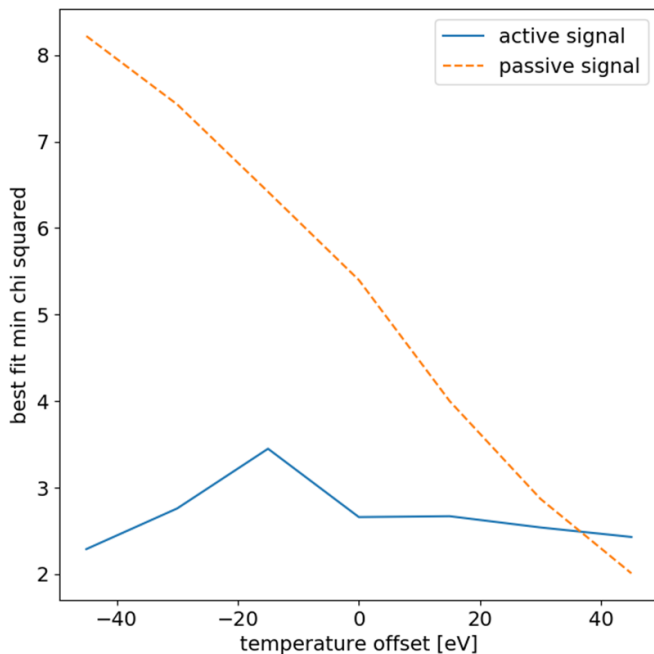


Figure 16. Best fit χ^2_{r} for various additional temperature offsets.

ORCID iDs

C Sweet  <https://orcid.org/0000-0003-2365-6777>

B Geiger  <https://orcid.org/0000-0001-8706-1874>

A Bader  <https://orcid.org/0000-0002-6003-374X>

References

- [1] Coster D P, Schneider R, Neuhauser J, Braams B and Reiter D 1996 Theory and modelling of time dependent phenomena in the plasma edge *Contrib. Plasma Phys.* **36** 150–60
- [2] Canik J M, Anderson D T, Anderson F S B, Likin K M, Talmadge J N and Zhai K 2007 Experimental demonstration of improved neoclassical transport with quasihelical symmetry *Phys. Rev. Lett.* **98** 085002
- [3] Faber B J, Pueschel M J, Proll J H E, Xanthopoulos P, Terry P W, Hegna C C, Weir G M, Likin K M and Talmadge J N 2015 Gyrokinetic studies of trapped electron mode turbulence in the helically symmetric experiment stellarator *Phys. Plasmas* **22** 072305
- [4] Geiger B *et al* 2019 Observation of anomalous impurity transport during low-density experiments in W7-X with laser blow-off injections of iron *Nucl. Fusion* **59** 046009
- [5] Zhou Q, Sang C, Xu G, Ding R, Zhao X, Wang Y and Wang D 2020 The transport of tungsten impurities induced by the intrinsic carbon during upper-single null discharge on east tokamak *Nucl. Mater. Energy* **25** 100849
- [6] Sciortino F *et al* 2020 Inference of experimental radial impurity transport on Alcator C-mod: Bayesian parameter estimation and model selection *Nucl. Fusion* **60** 126014
- [7] Langenberg A *et al* 2017 Argon impurity transport studies at Wendelstein 7-X using x-ray imaging spectrometer measurements *Nucl. Fusion* **57** 086013
- [8] Dux R 2018 *STRAHL User Manual* (Max-Planck-Institut für Plasmaphysik)
- [9] Summers H P 2004 *The Adas User Manual*
- [10] Feng Y, Sardei F, Kisslinger J and Grigull P 1997 A 3d Monte Carlo code for plasma transport in island divertors *J. Nucl. Mater.* **241–243** 930–4
- [11] Heidbrink W W, Liu D, Luo Y, Ruskov E and Geiger B 2011 A code that simulates fast-ion $d\alpha$ and neutral particle measurements *Commun. Comput. Phys.* **10** 716–41
- [12] Geiger B *et al* 2020 Progress in modelling fast-ion D-alpha spectra and neutral particle analyzer fluxes using FIDASIM *Plasma Phys. Control. Fusion* **62** 07
- [13] Geiger B, Edmondson A, Gerard M, Henning L, Kumar S T A, Poloskei P and Sweet C 2021 pyFIDASIM simulations of the neutral density and charge-exchange losses in the HSX stellarator *TTF Conf. Proc.* vol 2021
- [14] Mohoney J M, Kumar S T A, Likin K M and Anderson D T 2017 Carbon impurity measurements in the HSX stellarator *APS Division of Plasma Physics Meeting Abstracts, vol. 2017 of APS Meeting Abstracts* p CP11.079
- [15] Briesemeister A R 2013 Measurement and modeling of the flows and radial electric field in the HSX stellarator *PhD Thesis* The University of Wisconsin, Madison
- [16] Spong D A 2005 Generation and damping of neoclassical plasma flows in stellarators *Phys. Plasmas* **12** 056114
- [17] Kumar S, Talmadge J, Dobbins T, Anderson F, Likin K and Anderson D 2017 Determination of radial electric field from Pfirsch–Schlüter flows in the HSX stellarator *Nucl. Fusion* **57** 036030
- [18] Dux R, Cavedon M, Kallenbach A, McDermott R, Vogel G and Upgrade team the A S D E X 2020 Influence of CX-reactions on the radiation in the pedestal region at ASDEX upgrade *Nucl. Fusion* **60** 126039
- [19] Helander P and Zocco A 2018 Quasilinear particle transport from gyrokinetic instabilities in general magnetic geometry *Plasma Phys. Control. Fusion* **60** 084006
- [20] Marushchenko N, Turkin Y and Maassberg H 2014 Ray-tracing code TRAVIS for ECR heating, EC current drive and ECE diagnostic *Comput. Phys. Commun.* **185** 165–76
- [21] Weir G, Likin K, Marushchenko N and Turkin Y 2015 Ray tracing and ECRH absorption modeling in the HSX stellarator *Nucl. Fusion* **55** 113011
- [22] Ryter F *et al* 2006 Electron heat transport studies *Plasma Phys. Control. Fusion* **48** B453–63
- [23] Gravier E, Lesur M, Garbet X, Sarazin Y, Médina J, Lim K and Idouakass M 2019 Diffusive impurity transport driven by trapped particle turbulence in tokamak plasmas *Phys. Plasmas* **26** 082306
- [24] Skyman A, Nordman H and Strand P 2012 Particle transport in density gradient driven TE mode turbulence *Nucl. Fusion* **52** 114015